Chemical Science

ROYAL SOCIETY OF CHEMISTRY

EDGE ARTICLE

View Article Online
View Journal | View Issue

Cite this: *Chem. Sci.*, 2025, **16**, 16293

All publication charges for this article have been paid for by the Royal Society of Chemistry

Biasing the polymorphism of a semicrystalline covalent polymer by exploiting the microstructure of supramolecular copolymers

Alexi Riba-Bremerch,[a] Arnaud Y.-G. Delplanque,[a] Clément Guibert [b] and Nathan J. Van Zee *[a]

Received 10th April 2025
Accepted 5th August 2025

DOI: 10.1039/d5sc02678d

rsc.li/chemical-science

Supramolecular copolymers constitute a promising class of modular and dynamic materials. While most efforts thus far have been focused on tailoring their synthesis, structure, and function, their ability to impose order on the surrounding matrix remains poorly understood and relatively unexploited. In this context, we were intrigued by the potential of supramolecular copolymers to guide the outcome of the liquid–solid phase transition of a matrix. We hypothesized that the microstructure of a supramolecular copolymer could influence the local ordering of matrix molecules in the liquid state as it is cooled and solidified, thereby dictating its solid-state structure. Herein, we exemplify this concept using a matrix of isotactic polypropylene (PP) and supramolecular copolymers based on benzene tricarboxamides (BTAs). Two BTA structures were chosen for this study, one that exclusively nucleates the α-form of PP and another that preferentially nucleates the β-form. We demonstrate that the stoichiometric imbalance of the BTA comonomers and their microstructure within the copolymer play crucial roles in biasing the crystallization of the matrix.

Introduction

One-dimensional supramolecular copolymerization is a powerful approach for creating dynamic functional materials.[1–3] Incredible progress has been made in the design of comonomers and the synthetic strategies for assembling them together.[4] While most recent efforts have been focused on tailoring the synthesis, structure, and function of supramolecular copolymers,[5–27] many intriguing questions persist, such as the interactions between the supramolecular copolymer and the molecules that make up the matrix. As an example, Stupp and co-workers[28,29] have reported a large family of peptide amphiphile-based (co)polymer networks to make functional hydrogels; they have demonstrated the retardation of the dynamics of water molecules in proximity to the peptide amphiphile structure.[30] The Meijer group[31] recently reported synthetic tactoids composed of supramolecular copolymers that induce liquid–liquid phase separation in water. Aida and co-workers[32–35] have designed one-dimensional supramolecular polymers that coassemble with a nematic liquid crystalline matrix, which remarkably leads to the formation of a single columnar mesophase.

The ability of supramolecular copolymers to orchestrate the organization of matrix molecules nevertheless remains poorly understood. This gap of understanding likely exists because most supramolecular copolymers are formulated in low molecular weight solvents in the liquid phase. Although the influence of the solvent properties on supramolecular polymer structure has been deeply investigated,[36,37] it is challenging to elucidate transient structuration of the solvent molecules owing to the relatively short lifetime of such interactions. These considerations sparked our interest in the potential impact of supramolecular copolymers on liquid–solid phase transitions. Assuming that the structure of a supramolecular copolymer influences the local ordering of the matrix molecules in the liquid state, we hypothesized that these interactions could have a profound impact on the structuration of the matrix as it is cooled and solidified. Aside from being comparatively easier to study the structure of materials in the solid state, we anticipated that this insight could be valuable for practical applications, ranging from organic semi-conductors[38] to commodity plastics.[39]

We were inspired by one of the few current commercial applications of supramolecular polymers: nucleating agents for semicrystalline polymers. Supramolecular polymers are commonly applied to isotactic polypropylene (PP), which is today one of the most widely-produced semicrystalline polymers. PP exhibits relatively slow crystallization kinetics, necessitating the use of such additives in many commercial products.[39] When PP is cooled from the melt, the polymer

[a]*Chimie Moléculaire, Macromoléculaire, Matériaux, ESPCI Paris, Université PSL, CNRS, 75005 Paris, France. E-mail: nathan.van-zee@espci.psl.eu*

[b]*Sorbonne Université, CNRS, Laboratoire de Réactivité de Surface, F-75005 Paris, France*

chains adopt a three-fold helical conformation that pack in different ways according to the processing conditions and the structure of the supramolecular polymer. PP exhibits rich polymorphism—its two most common crystal morphologies, the monoclinic α-form and trigonal β-form, are schematically depicted in Fig. 1A.[40]

Among the many kinds of additives used to nucleate the crystallization of PP, those based on supramolecular polymers of benzene tricarboxamides (BTAs) are intriguing because the structure of the side groups dictates their polymorph selectivity. Kristiansen, Smith, Schmidt, and co-workers[41–44] reported that the isopentyl derivative **a** and the *tert*-octyl derivative **b** (Fig. 1B) assemble into bundles of fibers in molten PP and nucleate the α- and β-forms, respectively, with high selectivity (Fig. 1C). It is proposed that the BTA polymers influence the morphology of PP *via* epitaxial crystallization,[45] which is possible when there is matching between the periodic structure of the BTA polymer and the dimensions of a PP crystal morphology. Indeed, the double of the interdisc distance between two BTA units is approximately 6.7 Å (Fig. 1C), which is close to the spacing between PP chains in both the crystalline α- and β-forms (Fig. 1A). The reason for BTAs **a** and **b** to nucleate different

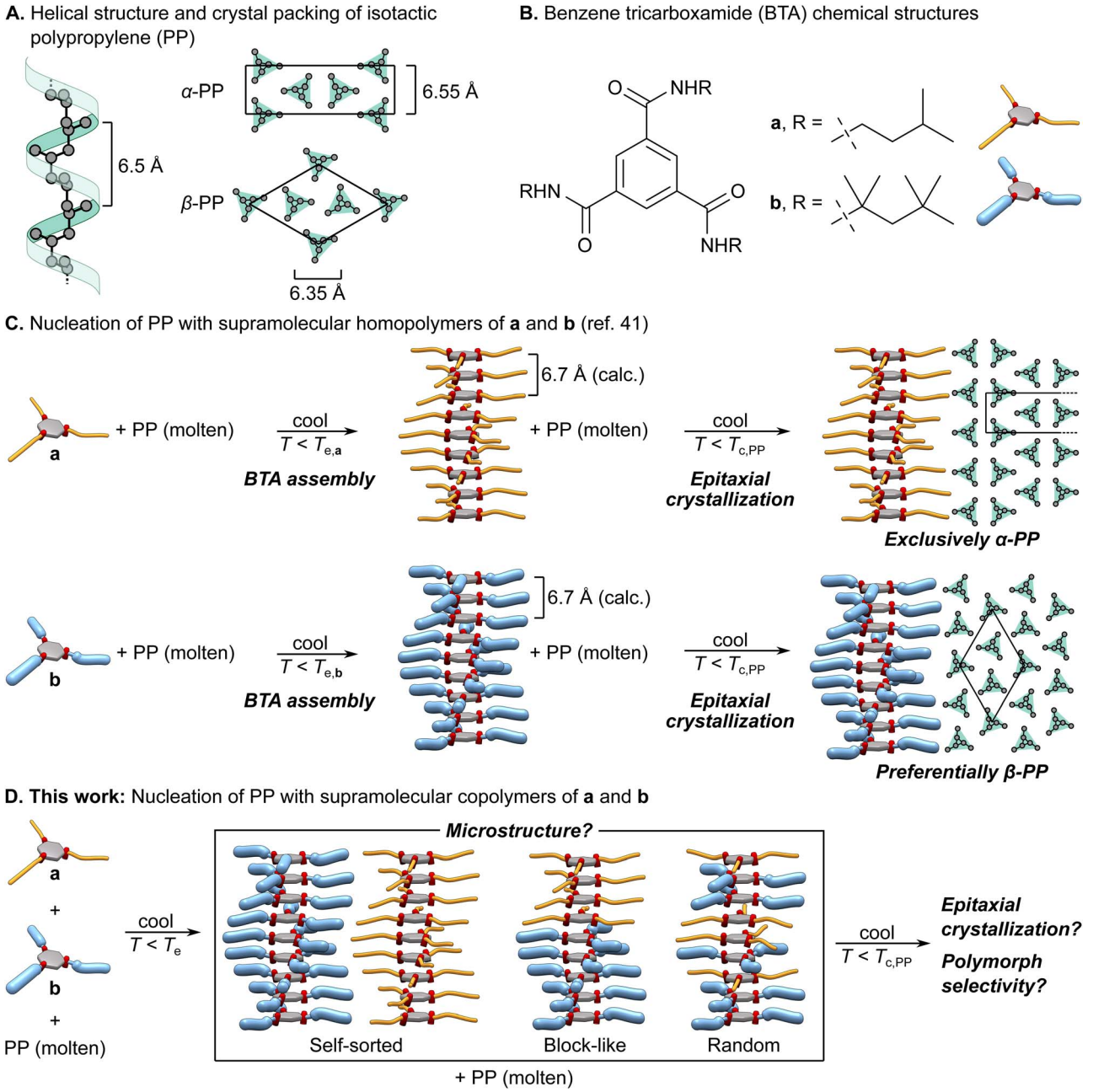

Fig. 1 (A) Helical structure and crystal packing of isotactic polypropylene (PP).[40] (B) Chemical structure of benzene tricarboxamides (BTAs) **a** and **b**. (C) Schematic representation of the supramolecular homopolymerization and the nucleation of the PP matrix.[41] (D) Schematic representation of the supramolecular copolymerization of **a** and **b** and nucleation of PP.

morphisms of PP has not yet been unambiguously resolved,[46] but, based on studies of other systems,[47,48] the side chains likely impart subtle differences to the periodic surface texture of the supramolecular structure that influence the organization of the PP chains.

Herein, we exploit the contrasting nucleating properties of BTAs **a** and **b** to exemplify how supramolecular copolymers dictate the polymorphism of PP as it undergoes a liquid–solid phase transition (Fig. 1D). Previous reports of using mixtures of supramolecular polymers, among other kinds of additives, to nucleate covalent polymer crystallization have overlooked the profound implications of possible supramolecular copolymerization.[42,49–58] We find that the stoichiometric imbalance of the BTA comonomers and their microstructure within the copolymer play crucial roles in biasing the crystallization of the matrix.

Results and discussion

Supramolecular homopolymerization of benzene tricarboxamides (BTAs) in polypropylene (PP)

BTAs **a** and **b** were synthesized according to literature protocols.[41] Based on several comprehensive studies by Schmidt and co-workers,[46,59,60] **a** and **b** are crystalline solids at room temperature, and they assemble *via* three-fold hydrogen bonding into well-ordered one-dimensional columns that laterally aggregate into disordered bundles. Both **a** and **b** exhibit a plastic crystalline mesophase when heated to 211 and 281 °C, respectively, and then the optically isotropic state (*i.e.*, short columns of stacked BTAs that do not exhibit birefringence) at 272 and 317 °C, respectively.

For the present study, varying amounts of **a** or **b** were mixed with molten PP using a twin-screw micro-compounder according to a solvent-free protocol that is detailed in the SI. The concentration of the BTAs was set to be sufficiently high to facilitate the study of the supramolecular (co)polymerization but low enough to avoid liquid–liquid phase separation at high temperatures. Kristiansen, Smith, Schmidt, and co-workers[41,44] previously reported temperature/composition diagrams for **a** in PP, and they found that **a** forms homogeneous mixtures with molten PP at high temperatures at loadings below approximately 2 wt%, which corresponds to 49 mmol of **a** per kg of PP (Fig. S7). Similar behavior was also reported for BTA **b**.[41] Samples throughout this study are named according to the millimolality of each BTA component. For example, **PP-a$^{9.2}$** contains 9.2 mmol of **a** per kg of PP.

When **PP-a$^{9.2}$** and **PP-b$^{9.2}$** were cooled from high temperature, imaging by polarized optical microscopy (POM) revealed that **a** homopolymerized to form long needle-like structures (Fig. 2A), while **b** formed a dendritic network of relatively thinner fibers (Fig. 2E). The fact that both structures were visible by optical microscopy indicates that both BTAs formed bundles of fibers. The assembly of the BTAs was corroborated by rheological measurements (Fig. S20), where an abrupt increase in complex viscosity while cooling from high temperature indicated the formation of a network of supramolecular polymers in the PP matrix.

The formation of these polymers was quantitatively assessed by variable-temperature Fourier-transform infrared (VT-FTIR) spectroscopy. Achieving the molecularly isotropic state of **a** and **b** in PP at high temperature was confirmed by the shift of the N–H stretching band to 3447–3472 cm^{-1} (Fig. S11).[59] The amide I bands of molecularly-dissolved **a** and **b** in **PP-a$^{9.2}$** and **PP-b$^{9.2}$** (Fig. 2B and F, respectively) were both identified at 1684 cm^{-1}. Upon cooling at −1 °C min^{-1} to each respective elongation temperature (T_e'), the absorbance of the monomer band rapidly decreased while the absorbance of a new band at 1637 cm^{-1}, the amide I band of polymerized BTA, concomitantly increased. Samples were cooled to 155 °C (*i.e.*, low enough to fully polymerize the BTA but high enough to prevent PP crystallization) and then heated at +1 °C min^{-1} to observe the depolymerization process.

For quantifying the polymerization as a function of temperature, the spectroscopic data were converted into cooling and heating curves based on the intensity of the polymer amide I band (Fig. 2C and G). To minimize the impact of experimental variations across different measurements (*e.g.*, due to variability in the measurement of sample thickness), the change in intensity of the polymer band was defined as a ratio between it and the intensity of the monomer band at high temperature when the BTAs are fully disassembled. Thus, the polymerization and depolymerization of the BTAs are expressed as $\Delta A_{1637}/\Delta A_{1684,HT}$ (eqn (S1)), where ΔA_{1637} is the baseline-subtracted intensity of the polymer band at 1637 cm^{-1} and $\Delta A_{1684,HT}$ is the baseline-subtracted intensity of the monomer band at 1684 cm^{-1} measured at approximately 5 °C above the elongation temperature (Fig. S2).

Based on the non-sigmoidal shape of the heating curves in Fig. 2C and G, **a** and **b** supramolecularly polymerized *via* a nucleation-elongation mechanism, which can be described using a well-established mass-balance model developed by ten Eikelder and Markvoort.[61–63] This theoretical framework is advantageous because it is a direct, computationally efficient approach for gaining insight into the microstructure of such systems. It is important to note that this model is only valid for systems under thermodynamic control. For the homopolymerization of **a** and **b**, it was thus necessary to address two nuances to justify the implementation of this approach: the hysteresis between the heating and cooling curves as well as the apparent structural transition in the homopolymerization of **a**.

First, although the cooling and heating curves for **PP-a$^{9.2}$** and **PP-b$^{9.2}$** are close to overlapping at temperatures below 200 °C with a temperature ramp of 1 °C min^{-1}, there is a large hysteresis near the elongation temperatures. For **a** in **PP-a$^{9.2}$**, an undercooling (*i.e.*, $\Delta T = T_e - T_e'$, where T_e and T_e' are the elongation temperatures upon heating and cooling, respectively) of approximately 12 °C was observed. For **b** in **PP-b$^{9.2}$**, ΔT under the same conditions was 20 °C. The magnitude of the hysteresis was larger with faster temperature ramps (2.5 and 5 °C min^{-1}, see Fig. S12 and S13). This behavior is indicative of a kinetic barrier for the formation of nuclei, which delays the formation of supramolecular polymers.[64] To illustrate the timescale associated with this barrier, a kinetic isothermal experiment was performed in which the polymerization of **b** was monitored by

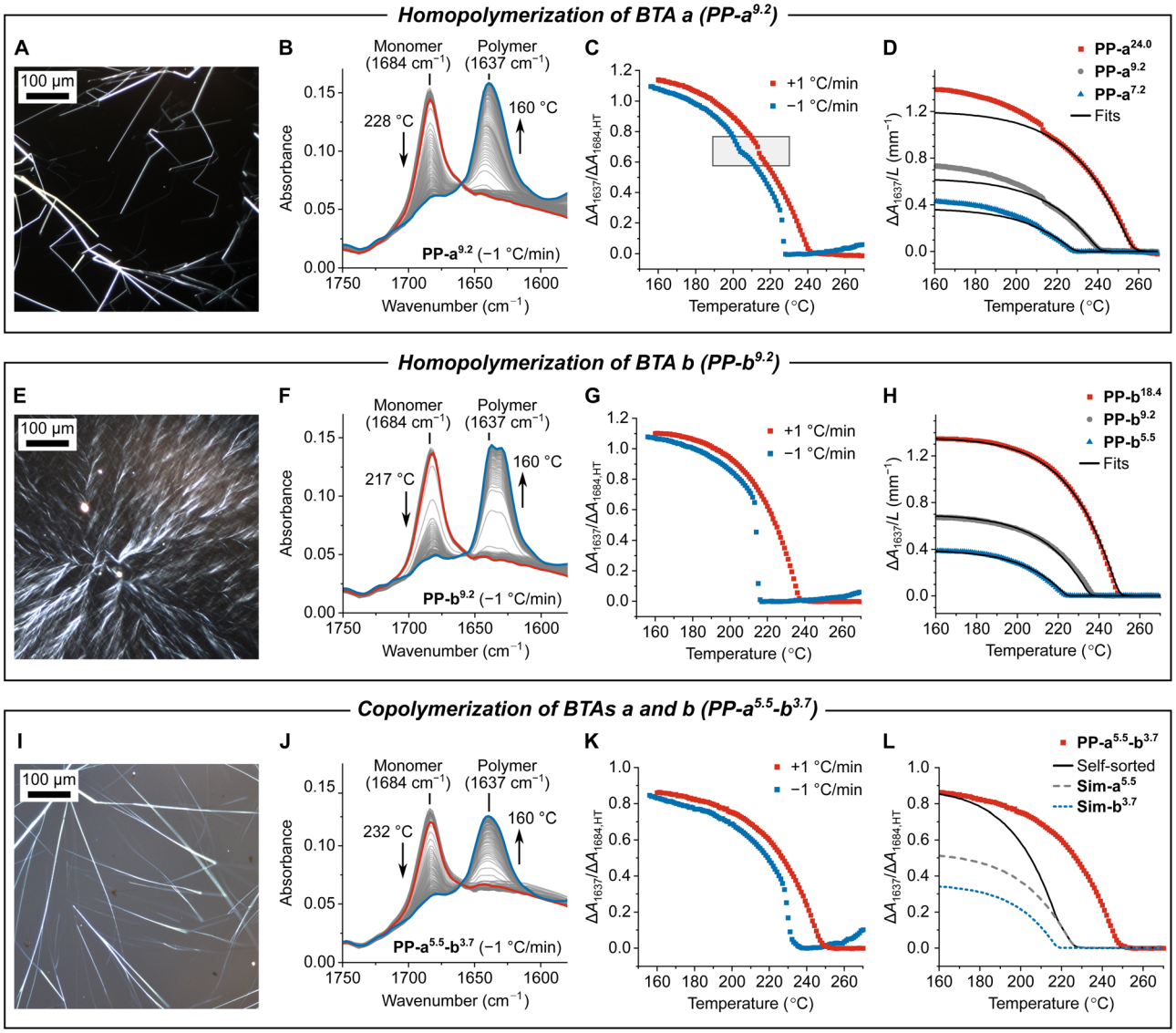

Fig. 2 (A, E and I) Polarized optical microscopy (POM) images upon cooling each sample to 180 °C from 260 °C at −1 °C min^{-1}. (B, F and J) Variable temperature Fourier-transform infrared (VT-FTIR) spectra. (C, G and K) Cooling and heating curves that follow the polymerization and depolymerization processes, respectively. In part (C), the conformational change observed in **PP-a$^{9.2}$** is indicated by a grey box. (D and H) Simulations and fitting of the heating curves acquired at +1 °C min^{-1}. Experimental data are represented as colored symbols, while fits are shown as solid black lines. (L) Experimental heating curve of **PP-a$^{5.5}$-b$^{3.7}$** plotted with simulated curves corresponding to the supramolecular depolymerization of self-sorted **a** and **b** homopolymers.

FTIR spectroscopy in **PP-b$^{9.2}$** after cooling the sample rapidly to 225 °C (*i.e.*, between T_e and T_e', see Fig. S14). After a 4.5 h inhibition period, **b** finally began to polymerize, with the intensity of the signal slowly increasing over the subsequent 6 h. We thus applied the mass-balance model to the heating curves of the homopolymerization of **a** and **b** acquired at +1 °C min^{-1}. We assumed that the homopolymerization processes were sufficiently close to thermodynamic equilibrium at this rate. The depolymerization on the heating cycle is a thermodynamically-controlled process because it does not entail a kinetically-controlled nucleation step as on the cooling cycle.[65]

Second, the heating and cooling curves for the polymerization of **a** revealed a transition at approximately 220 and 205 °C, respectively (see grey box in Fig. 2C). This transition was also apparent with faster temperature ramps (Fig. S12). However, it could not be observed in the cooling and heating curves depicting the evolution of the monomer concentration at 1684 cm^{-1} (Fig. S15), suggesting that this transition is due to a subtle conformational change of the homopolymer. This hypothesis was corroborated by a small shift in the peak maximum of the polymer band by VT-FTIR spectroscopy (Fig. S16), as well as a transition detected by variable temperature wide-angle X-ray scattering (VT-WAXS, reflections labelled a and b–d in Fig. S17). We noted that no comparable structural transitions were observed for the polymerization of **b** (Fig. S16, S18, and S19). Thus, for the homopolymerization of **a**, only the thermodynamics of the assembly process at high temperature was considered; a similar strategy was applied to model the

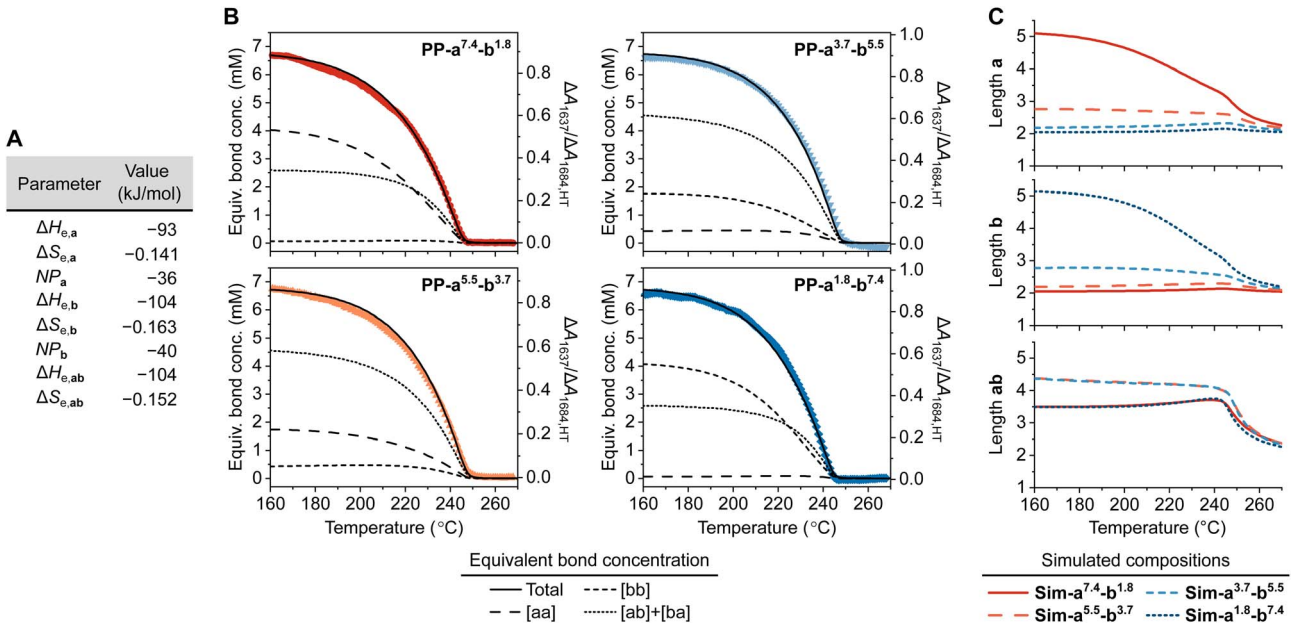

Fig. 3 (A) Thermodynamic parameters calculated by fitting experimental data to the mass-balance model of ten Eikelder and Markvoort.[61–63] (B) Experimental heating curves acquired at +1 °C min^{-1} (colored symbols) and simulated curves (black solid and dashed lines) calculated using the mass-balance model. (C) Simulated weight-average block lengths as a function of temperature.

supramolecular copolymerization of triphenylamine tricarboxamides.[62]

The calculated curves for three different concentrations of **a** and **b** in PP are presented in Fig. 2D and H. For these samples, the experimental data was normalized as $\Delta A_{1637}/L$, where L is the sample thickness. The theoretical curves matched very well with the experimental depolymerization data of each homopolymer. The resulting thermodynamic parameters are presented in Fig. 3A. In short, the homopolymerization of **b** was more exothermic (enthalpy of elongation, ΔH_e, of −104 *versus* −93 kJ mol^{-1}) and slightly more cooperative (nucleation penalty, NP, of −40 *versus* −36 kJ mol^{-1}) than the homopolymerization of **a**.

The values of ΔH_e calculated for **a** and **b** in PP are significantly more exothermic than typical values of similar BTAs in solvent. For comparison, a BTA derivative with three *n*-octyl groups in methylcyclohexane displayed an ΔH_e of −60.1 kJ mol^{-1} using the mass-balance model.[66] We attribute this discrepancy of exothermicity to the ability of BTAs **a** and **b** to form strong macrodipoles.[60] The more compact bulky side groups of **a** and **b** enhance their ability to assemble into well-ordered columns[67] compared to typical BTAs studied in apolar solvents.[68] Moreover, Kulkarni *et al.*[69,70] has shown that the formation of macrodipoles can dramatically enhance the thermodynamic favorability of one-dimensional supramolecular polymerization.

Supramolecular copolymerization of BTAs in PP

Four compositions were prepared that contained a mixture of BTAs **a** and **b** in PP. The total BTA concentration was fixed at 9.2 mmol per kg of PP, and the **a** : **b** molar ratios were set to 4 : 1, 3 : 2, 2 : 3 and 1 : 4, giving the compositions **PP-a$^{7.4}$-b$^{1.8}$**, **PP-a$^{5.5}$-b$^{3.7}$**, **PP-a$^{3.7}$-b$^{5.5}$**, and **PP-a$^{1.8}$-b$^{7.4}$**, respectively. As a representative example, the properties of **PP-a$^{5.5}$-b$^{3.7}$** will be considered in detail (Fig. 2I–L and S21–S23), and the results for the other mixtures are provided in the SI (Fig. S24–S31). The copolymerization of **a** and **b** in PP resulted in the formation of long needle-like structures (Fig. 2I), similar in size and shape to those of the homopolymer of **a** (Fig. 2A). Rheological measurements revealed that the formation of these structures coincided with a sharp increase in the complex viscosity of the material, indicating the formation of a network structure (Fig. S20). Based on VT-FTIR measurements, the amide I band assigned to the formation of the copolymer appeared at the same wavenumber as the homopolymers, 1637 cm^{-1} (Fig. 2J).

As can be seen in the heating and cooling curves (Fig. 2K and S21), an undercooling ΔT of 18 °C was observed with a temperature ramp of 1 °C min^{-1}. The hysteresis was small below 180 °C and more prominent with faster temperature ramps (Fig. S22). Interestingly, the T_e and T_e' values for **PP-a$^{5.5}$-b$^{3.7}$** were both higher than those observed for the homopolymers in **PP-a$^{9.2}$** and **PP-b$^{9.2}$**, which is a first indication of supramolecular copolymerization. This hypothesis was further reinforced by comparing the experimental heating curve of **PP-a$^{5.5}$-b$^{3.7}$** with a simulated self-sorted heating curve, which was constructed by summing the simulated homopolymerization heating curves of **a** and **b** at concentrations of 5.5 and 3.7 mmol kg^{-1}, respectively (Fig. 2L). The smooth shape of the experimental curve, along with the large discrepancy between the T_e values for the experimental and simulated curves, are fully consistent with the formation of a supramolecular copolymer.[1]

Measurements by VT-WAXS provided further evidence of supramolecular copolymerization. Homopolymers of **a** in **PP-a$^{9.2}$** exhibited three reflections near a q of 0.5 Å^{-1} corresponding to d-spacings of 13.6, 13.2, and 12.6 Å (Fig. S17). The

homopolymers of **b** in **PP-b**$^{9.2}$ displayed three reflections near a q value of 0.4 Å^{-1}, corresponding to larger d-spacings (15.3, 14.9, and 14.4 Å; Fig. S19). Strikingly, the supramolecular copolymer formed in **PP-a**$^{5.5}$**-b**$^{3.7}$ exhibited a single reflection at this length scale with a d-spacing of 14.0 Å, which is in between those of the homopolymers. The precise molecular structures of the homo- and copolymers in PP remain unknown, thus precluding the formal assignment of these signals. Nevertheless, comparison with other BTAs reported in the literature suggest that this dimension is related to the lateral spacing of the BTA fibers.[59,71,72] For comparison, based on molecular models calculated using semi-empirical quantum chemical methods, tetramers of **a** and **b** have diameters of approximately 17 and 18 Å, respectively (Fig. S32 and S33).

The other copolymers prepared with different ratios of **a** and **b** all exhibited similar degrees of undercooling and elevated elongation temperatures compared to the supramolecular homopolymerization of **a** and **b** (Fig. S24–S27). All copolymers formed needle-like structures as visualized by POM (Fig. S27). Finally, the copolymers exhibited similar diagnostic reflections based on VT-WAXS measurements with progressively larger d-spacing as the fraction of the bulkier comonomer **b** was increased (13.9, 14.2 and 14.7 Å for **PP-a**$^{5.5}$**-b**$^{3.7}$, **PP-a**$^{3.7}$**-b**$^{5.5}$, and **PP-a**$^{1.8}$**-b**$^{7.4}$, respectively, see Fig. S28–S31).

Simulation of supramolecular copolymerization reveals the microstructure

To elucidate the microstructure of the copolymers formed in **PP-a**$^{7.4}$**-b**$^{1.8}$, **PP-a**$^{5.5}$**-b**$^{3.7}$, **PP-a**$^{3.7}$**-b**$^{5.5}$, and **PP-a**$^{1.8}$**-b**$^{7.4}$, the experimental heating curves were simulated using the supramolecular copolymerization mass-balance model of ten Eikelder and Markvoort.[62] The thermodynamic parameters for the homopolymerization of **a** and **b** (Fig. 3A) were used as inputs for these calculations. Concerning the thermodynamic parameters of the **ab** heterointeractions, the entropy of elongation ($\Delta S_{e,ab}$) was taken as the average of $\Delta S_{e,a}$ and $\Delta S_{e,b}$ (−0.152 kJ mol^{-1}). The enthalpy of elongation ($\Delta H_{e,ab}$) was iteratively screened (Fig. S34); a close match between the experimental and simulated curves was achieved with a $\Delta H_{e,ab}$ value of −104 kJ mol^{-1}, which is equal to that of $\Delta H_{e,b}$ and lower than $\Delta H_{e,a}$. As can be seen in Fig. 3B, the simulations well-captured the trends of the T_e values and the shape of the experimental curves.

These calculations provide valuable insight into the microstructure of the supramolecular copolymers. To facilitate the discussion, comparisons were made between the simulated compositions at 160 °C, at which over 98% of the monomers are incorporated into the supramolecular copolymers. As expressed in the equivalent bond concentration plots, the copolymer formed in **PP-a**$^{7.4}$**-b**$^{1.8}$ was comprised of predominantly **aa** (60%) and **ab** (39%) units; less than 1% were **bb** units. For **PP-a**$^{5.5}$**-b**$^{3.7}$, which has a molar ratio of **a** and **b** closer to unity, the copolymer was made up mostly **ab** units (68%), followed by **aa** (26%) and **bb** (6%) units. As the loading of **b** was increased in **PP-a**$^{3.7}$**-b**$^{5.5}$ and **PP-a**$^{1.8}$**-b**$^{7.4}$, the fraction of **bb** units continued to increase, going from 26 to 61%, respectively.

Through simulation of the copolymerization processes, the model also permitted the calculation of the weight-average

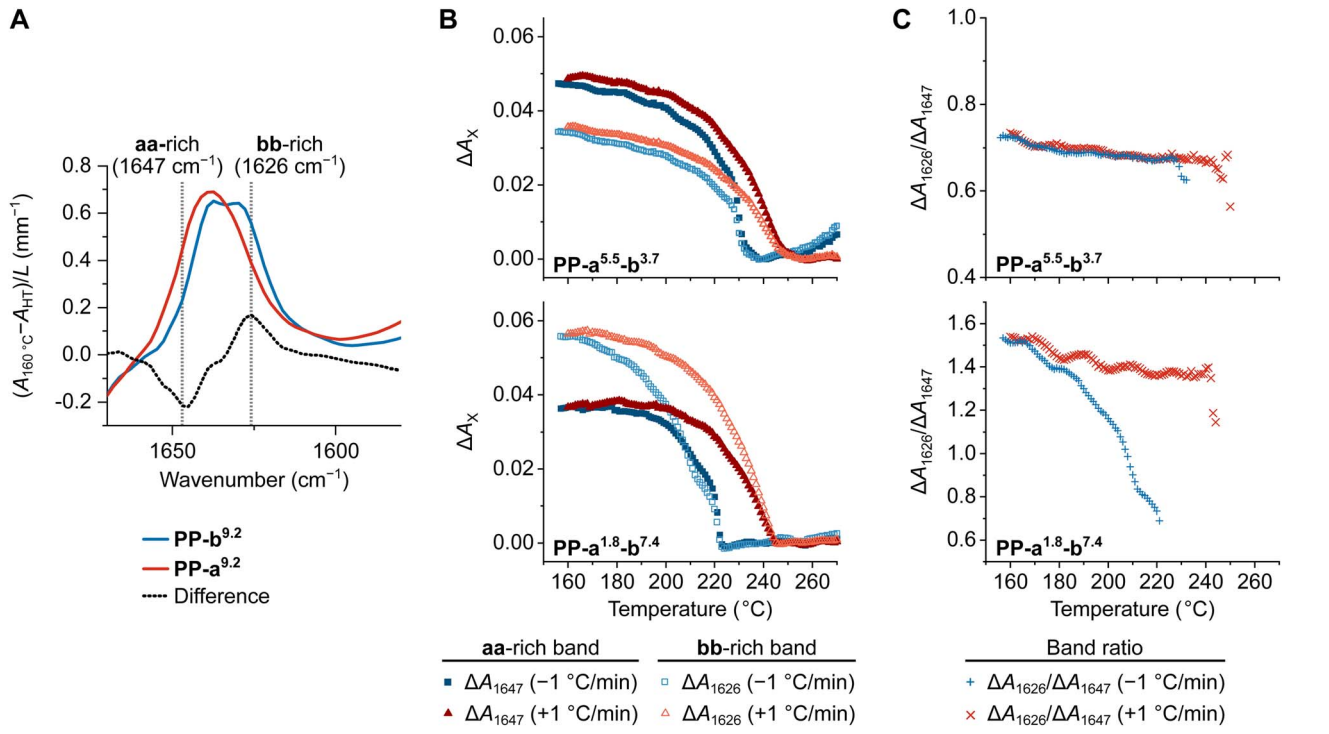

Fig. 4 (A) Subtracted spectra for the supramolecular homopolymers at 160 °C, normalized by the thickness of the sample, L. The difference between these two spectra is indicated by a dashed line. (B) The intensity of the **aa**-rich and **bb**-rich bands as a function of temperature for **PP-a**$^{5.5}$**-b**$^{3.7}$ and **PP-a**$^{1.8}$**-b**$^{7.4}$. (C) The corresponding ratio of these bands plotted as a function of temperature.

block lengths of **a**, **b**, and **ab** (*i.e.*, alternating) segments, which offered further perspective on the microstructure of these copolymers (Fig. 3C). The minimum block size considered in this framework is two monomer units. The average block lengths were directly dependent on the molar ratio of the monomer feed. For instance, in going from the **b**-poor composition **PP-a$^{7.4}$-b$^{1.8}$** to the **b**-rich composition **PP-a$^{1.8}$-b$^{7.4}$**, the **b** weight average block size increased from 2.0 (*i.e.*, the minimum value) to 5.1 units. Likewise, the weight average **a**-block size decreases from 5.0 to 2.0 units, representing the inverse trend.

The copolymers of **a** and **b** exhibit an essentially random microstructure because of the similar thermodynamic properties of the homo- and heterointeractions. However, this analysis reveals that small blocks are nevertheless formed by adjusting the monomer feed. A stronger monomer imbalance leads to the formation of larger blocks of homopolymer segments throughout the copolymer. Similar considerations are well-established for random copolymers prepared by conventional covalent polymerization methods.[73] Given that the nucleation of the PP matrix is driven by epitaxial crystallization, we posited that the nucleation properties of the copolymers would be dictated by these microstructural subtleties. Compositions rich in **b** would contain a significant fraction of **bb** segments with larger **bb** block sizes, rendering them more likely to promote the formation of β-PP (and reciprocally with compositions rich in **a** and formation of α-PP).

However, this microstructural analysis was performed on the heating curves, while the liquid–solid phase transition of the PP matrix takes place on cooling. Although the T_e' values for each copolymer were higher than those predicted for a self-sorted system (see Fig. S35 and S36 and the associated discussion in the SI), the copolymerization of **a** and **b** exhibits significant undercooling at all **a** : **b** ratios, which suggests that competitive kinetic effects could cause the microstructure to deviate from what was predicted under the assumption of thermodynamic control.

This point was addressed by careful analysis of the FTIR spectra of the supramolecular copolymers and comparing their composition upon cooling then heating. Based on the baseline-subtracted FTIR spectra of the homopolymers of **a** and **b**, we identified the bands at 1647 and 1626 cm^{-1} as being indicative of relatively **aa**- and **bb**-rich segments, respectively (Fig. 4A). It was not possible to satisfactorily decompose the contribution of these segments by peak fitting, but directly comparing the ΔA values at each frequency still provided valuable insights.

As representative examples, for **PP-a$^{5.5}$-b$^{3.7}$** and **PP-a$^{1.8}$-b$^{7.4}$**, we plotted these two bands (Fig. 4B) as well as the ratio between them (*i.e.*, $\Delta A_{1626}/\Delta A_{1647}$, Fig. 4C). In the case of **PP-a$^{5.5}$-b$^{3.7}$**, the heating and cooling curves of $\Delta A_{1626}/\Delta A_{1647}$ essentially overlapped, suggesting that the fraction of enchained **aa**- and **bb**-units followed a similar trend during polymerization and depolymerization. In contrast, for **PP-a$^{1.8}$-b$^{7.4}$**, the cooling curve for $\Delta A_{1626}/\Delta A_{1647}$ deviated from the heating curve at temperatures above 180 °C. Since the cooling curve was below the heating curve, it suggests that the copolymers during polymerization were relatively depleted in **bb**-segments compared to the copolymers during depolymerization. We hypothesize that this behavior is related to the relatively high kinetic barrier for BTA **b** to homopolymerize, which is likely due to the steric bulkiness of the *tert*-octyl side chains. The microstructure of **b**-rich copolymers was thus subject to a balance of the kinetics of elongation *versus* the dynamics of dissociation/reassociation of the enchained monomer units. We assume that the copolymers are sufficiently dynamic during slow cooling to allow for the microstructure to be well-predicted by modelling the depolymerization behavior on heating. The VT-WAXS measurements are consistent with this proposal (Fig. S23 and S28–S31), as they show that the copolymers are not a linear combination of homopolymerized **a** and **b** segments.

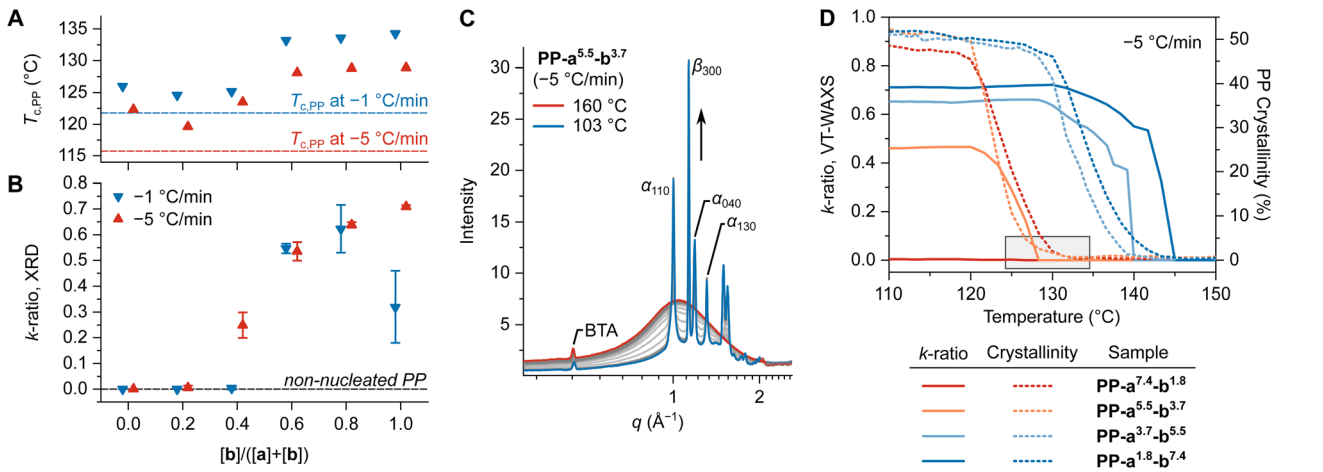

Fig. 5 (A) Crystallization temperature ($T_{c,PP}$) of the PP matrix as a function of composition. The full data set is presented in Fig. S42, S43, Tables S5 and S6. (B) The proportion of α- and β-PP expressed as the *k*-ratio based on X-ray diffraction measurements. (C) Variable temperature wide angle X-ray scattering (VT-WAXS) diffractograms. (D) The *k*-ratio and crystallinity of PP as a function of temperature as determined by VT-WAXS measurements. The full data set is presented in Fig. S44–S47. The grey box highlights the *k*-ratio at the onset of crystallization for **PP-a$^{5.5}$-b$^{3.7}$** (orange curves).

Biasing the polymorphism of the PP matrix

The impact of the BTA copolymers on the polymorphism of the PP matrix was studied while cooling molten samples below the crystallization temperature of PP, $T_{c,PP}$. To appreciate the behavior of the copolymers, it is useful to first consider that of the homopolymers. Compared to non-nucleated PP, **PP-a$^{9.2}$** exhibited $T_{c,PP}$ values that increased by 6.6 and 4.2 °C with cooling rates of −5 and −1 °C min^{-1}, respectively (Fig. 5A). According to *k*-ratios (*i.e.*, a relative measure of β-PP content, see eqn (S6) and Table S1 along with the related description in the SI) determined by X-ray diffraction measurements (XRD, Fig. 5B), the PP matrix exclusively crystallized in the α-form. The spherulites of α-PP in **PP-a$^{9.2}$** were significantly smaller than those observed in non-nucleated PP based on POM (Fig. 6, S37 and S38).

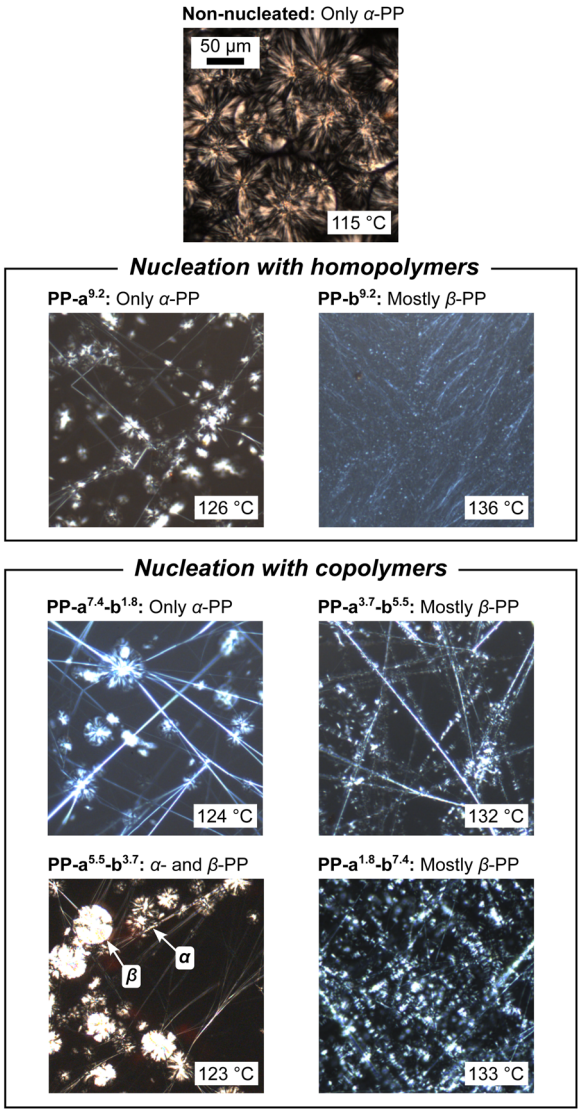

Fig. 6 POM images of non-nucleated and nucleated PP acquired while cooling each sample at −5 °C min^{-1}. The scale bar in the top image is the same for all other images.

In the case of **PP-b$^{9.2}$**, the $T_{c,PP}$ was increased even more by the BTA **b** homopolymers, raising it approximately 13 °C with both cooling rates (Fig. 5A). **PP-b$^{9.2}$** exhibited a *k*-ratio of approximately 0.7 at −5 °C min^{-1} and 0.3 at −1 °C min^{-1} (Fig. 5B). We hypothesize that this discrepancy is primarily related to the increased fiber thickness obtained at slower cooling rates (Fig. S39), which results in a lower BTA fiber surface area available for the nucleation of PP. Numerous small crystallites of β-PP were nucleated along the thin fibers of BTA **b** (Fig. 6 and S40).

The crystal morphologies of the PP matrix induced by the supramolecular copolymers were well in-line with our predictions from the microstructural analysis. For the compositions rich in BTA **a**, the copolymer formed in **PP-a$^{7.4}$-b$^{1.8}$** nucleated exclusively α-PP (Fig. 5B and 6), albeit with a lower efficiency than the BTA **a** homopolymer in **PP-a$^{9.2}$** based on DSC (Fig. 5A). Given the high concentration of **ab** units, low concentration of **aa** units, and near absence of **bb** units (Fig. 3B), we interpret this result as implying that the **ab** sequences have a relatively low efficiency for nucleating the PP matrix. The ability of BTA **b** to nucleate β-PP was suppressed by being primarily sequestered in the thermodynamically-favored **ab** segments.

In the case of **PP-a$^{5.5}$-b$^{3.7}$**, the $T_{c,PP}$ values were similar to that of **PP-a$^{9.2}$**, but DSC and XRD measurements revealed a tendency of the BTA copolymer of this composition to also nucleate β-PP. POM corroborated the nucleation of both α- and β-PP (Fig. 6 and S41B). Compared to the other BTA **b**-rich compositions (see below), the morphology of the β-PP domains was different, presenting itself as relatively large spherulites that were significantly more birefringent than the α-PP spherulites. This morphology has been reported in other PP samples where a β-nucleating agent is used in low concentration.[74]

We further investigated this point with VT-WAXS experiments. As shown in Fig. 5C, diffractograms were acquired as the sample was cooled at −5 °C min^{-1}. Upon reaching the $T_{c,PP}$, the characteristic diffraction peaks of α- and β-PP peaks emerged. The *k*-ratio, as well as the percent crystallinity of the PP matrix, were calculated for each diffractogram and plotted as a function of temperature in Fig. 5D. These experiments revealed that the copolymers in **PP-a$^{3.7}$-b$^{5.5}$** and **PP-a$^{1.8}$-b$^{7.4}$** had a high selectivity for the nucleation of β-PP from the onset of the crystallization of the matrix. In contrast, the copolymer of **PP-a$^{5.5}$-b$^{3.7}$** displayed an initial selectivity for α-PP that was accompanied by the latent nucleation of β-PP (Fig. 5D, grey box), which is in line with the other measurements by DSC, XRD, and POM. We propose that the faster rate of cooling (*i.e.*, −5 *versus* −1 °C min^{-1}) promoted the formation of more and/or longer **bb** homopolymer segments than predicted assuming thermodynamic control (Fig. 3B). Moreover, given that the growth rate of PP crystals in the β-form is faster than that of the α-form,[75] even a small amount of β-selective nucleation can result in a significant amount of β-PP in the solidified sample.

Finally, the compositions with copolymers rich in BTA **b**, **PP-a$^{3.7}$-b$^{5.5}$** and **PP-a$^{1.8}$-b$^{7.4}$**, displayed essentially the same value of $T_{c,PP}$ as **PP-b$^{9.2}$** (Fig. 5A). Both of these samples exhibited *k*-ratios of 0.55–0.65 at cooling rates of −1 and −5 °C min^{-1} (Fig. 5B), which are comparable to that of **PP-b$^{9.2}$**. Based on POM, despite

the strikingly different morphology of the two **b**-rich copolymers (needle-like structures) compared to the **b** homopolymer (thin dendritic fibers), β-PP formed on the surface of all three of these structures *via* epitaxial crystallization (Fig. 6, S41C and D).

It is remarkable that β-PP was nucleated by BTA copolymers constituted of relatively short **bb**-homopolymer segments that are interrupted by **aa** and **ab** segments (Fig. 3B and C). We draw several conclusions from this key result. Long BTA **b** homopolymer segments are not strictly required to impact the liquid–solid phase transition of the PP matrix. Moreover, assuming that the surface of **bb**-segments offers a unique periodic structure that promotes the formation of β-PP, this surface is conserved even when the **bb**-segments are dispersed through a copolymer structure. It remains notoriously difficult to predict the selectivity for how supramolecular polymers nucleate semicrystalline polymers,[45] but these results point toward the value of a modular approach grounded in the principles of supramolecular copolymerization.

Conclusions

In this work, we showcased how subtle changes in supramolecular copolymers can be translated and amplified to direct the structuration of the surrounding matrix. This concept was exemplified by exploiting supramolecular copolymers to dictate the polymorphism of PP, a semicrystalline covalent polymer. The comonomers used in this study, BTAs **a** and **b**, featured contrasting polymorph selectivity and were found to copolymerize with an essentially random microstructure. Relatively slow heating and cooling ramps permitted the use of a computationally efficient thermodynamic mass balance model to rationalize this microstructure. By employing a stoichiometric imbalance of comonomers, the formation of homopolymer sequences within the copolymer was thermodynamically favorable. These sequences engage in transient, multivalent interactions with PP chains in the liquid state, influencing their conformation and ultimately biasing the structure of the nuclei that then dictate the polymorphism of the solidified PP. This insight opens the door to rationally tuning the crystallization of polymers, offering a means to access specific morphologies for intermediate compositions.

This work bears a striking conceptual resemblance to the majority-rules and sergeants-and-soldiers principles.[76] These effects entail an imbalance in the concentration of a chiral monomer that gives rise to a structural consequence, which is the biased screw-sense of the resulting helical polymer. The strength of these effects is generally dictated by competitive thermodynamic parameters. In the present work, the relationship between the imbalance of monomer units and the structural consequences are spread across two components, the supramolecular copolymer and the organization of the surrounding matrix. In our exemplification, the structure of the supramolecular copolymer was well described assuming thermodynamic control with slow cooling, while the epitaxial crystallization and subsequent crystal growth of the PP matrix were intrinsically under kinetic control. We hope to further explore the consequences of kinetic effects on such systems in the future. We believe that this work highlights an important strategy for exploiting the microstructure of supramolecular copolymers not only to nucleate semicrystalline polymers but to generally access hierarchically structured materials.

Author contributions

A. Riba-Bremerch and A. Y.-G. Delplanque: conceptualization, data curation, formal analysis, investigation, methodology, visualization, writing – review & editing. C. Guibert: data curation, formal analysis, investigation, methodology, visualization, writing – review & editing. N. J. Van Zee: conceptualization, data curation, formal analysis, funding acquisition, investigation, methodology, project administration, supervision, visualization, writing – original draft, writing – review & editing.

Conflicts of interest

There are no conflicts to declare.

Data availability

The data supporting this article have been included in the SI. Additional data are available upon request from the corresponding author.

Materials and methods, benzene tricarboxamide (BTA) synthesis, sample preparation, SI characterization of BTA homopolymers and copolymers in polypropylene (PP), modelling of BTA homopolymers, fitting and simulation of spectroscopic data, SI analysis of copolymer microstructure, SI characterization of PP crystallization, and coordinates for the molecular models. See DOI: **https://doi.org/10.1039/d5sc02678d**.

Acknowledgements

This work was funded by the Agence Nationale de la Recherche through a JCJC grant (ANCHORS project, ANR-21-CE06-0008) and the City of Paris through the EMERGENCE program. The authors thank the SOLEIL Synchrotron (Saint-Aubin, FR) for financial support and an allocation of experimental time on the SWING beamline (proposal no. 20201245). Xplore, s.r.l. is gratefully acknowledged for performing the high temperature size exclusion chromatography measurement. The authors thank Mickaël Pomes-Hadda (ESPCI) for help in performing TGA measurements, François Tournilhac (ESPCI) for discussions and help with the FTIR spectroscopy measurements, and Renaud Nicolaÿ (ESPCI) for support and discussions. Beatrice Adelizzi (Danone) is kindly acknowledged for discussions and for the preparation of the three-dimensional graphics.

Notes and references

1 B. Adelizzi, N. J. Van Zee, L. N. J. de Windt, A. R. A. Palmans and E. W. Meijer, *J. Am. Chem. Soc.*, 2019, **141**, 6110–6121.
2 T. Aida and E. W. Meijer, *Isr. J. Chem.*, 2020, **60**, 33–47.

3 P. K. Hashim, J. Bergueiro, E. W. Meijer and T. Aida, *Prog. Polym. Sci.*, 2020, **105**, 101250.
4 B. Mu, Z. Gao, C. Liu, X. Xiao and W. Tian, *Chem. Commun.*, 2023, **59**, 5514–5530.
5 E. Moulin, J. J. Armao IV and N. Giuseppone, *Acc. Chem. Res.*, 2019, **52**, 975–983.
6 D. Bialas, E. Kirchner, M. I. S. Röhr and F. Würthner, *J. Am. Chem. Soc.*, 2021, **143**, 4500–4518.
7 Z. Fernandez, B. Fernandez, E. Quinoa and F. Freire, *J. Am. Chem. Soc.*, 2021, **143**, 20962–20969.
8 A. Sarkar, R. Sasmal, A. Das, A. Venugopal, S. S. Agasti and S. J. George, *Angew. Chem., Int. Ed.*, 2021, **60**, 18209–18216.
9 S. Sarkar, A. Sarkar, A. Som, S. S. Agasti and S. J. George, *J. Am. Chem. Soc.*, 2021, **143**, 11777–11787.
10 H. Su, S. A. H. Jansen, T. Schnitzer, E. Weyandt, A. T. Rosch, J. Liu, G. Vantomme and E. W. Meijer, *J. Am. Chem. Soc.*, 2021, **143**, 17128–17135.
11 L. N. J. de Windt, Z. Fernandez, M. Fernandez-Miguez, F. Freire and A. R. A. Palmans, *Chem.–Eur. J.*, 2022, **28**, e202103691.
12 R. Liao, F. Wang, Y. Guo, Y. Han and F. Wang, *J. Am. Chem. Soc.*, 2022, **144**, 9775–9784.
13 S. Takahashi and S. Yagai, *J. Am. Chem. Soc.*, 2022, **144**, 13374–13383.
14 S. Chakraborty, C. M. Berac, M. Urschbach, D. Spitzer, M. Mezger, P. Besenius and T. Speck, *ACS Appl. Polym. Mater.*, 2022, **4**, 822–831.
15 O. S. Stach, K. Breul, C. M. Berac, M. Urschbach, S. Seiffert and P. Besenius, *Macromol. Rapid Commun.*, 2022, **43**, e2100473.
16 A. Isobe, T. Kajitani and S. Yagai, *Angew. Chem., Int. Ed.*, 2023, **62**, e202312516.
17 P. Khanra, A. K. Singh, L. Roy and A. Das, *J. Am. Chem. Soc.*, 2023, **145**, 5270–5284.
18 L. Kleine-Kleffmann, V. Stepanenko, K. Shoyama, M. Wehner and F. Wurthner, *J. Am. Chem. Soc.*, 2023, **145**, 9144–9151.
19 H. Kong, Y. Li, A. Hammoud, L. Dubreucq, C. Troufflard, R. Maruchenko, L. Bouteiller and M. Raynal, *Chem.–Eur. J.*, 2023, **1**, e202300027.
20 L. López-Gandul, A. Morón-Blanco, F. García and L. Sánchez, *Angew. Chem., Int. Ed.*, 2023, **62**, e202308749.
21 R. Chen, A. Hammoud, P. Aoun, M. A. Martinez-Aguirre, N. Vanthuyne, R. Maruchenko, P. Brocorens, L. Bouteiller and M. Raynal, *Nat. Commun.*, 2024, **15**, 4116.
22 H. Kong, A. Valverde-Gonzalez, R. Maruchenko, L. Bouteiller and M. Raynal, *Angew. Chem., Int. Ed.*, 2024, e202421991.
23 S. Kotha, R. Sahu, A. C. Yadav, P. Sharma, B. Kumar, S. K. Reddy and K. V. Rao, *Nat. Commun.*, 2024, **15**, 3672.
24 A. J. Schwalb, F. García and L. Sánchez, *Chem. Sci.*, 2024, **15**, 8137–8144.
25 Y. Xue, Y. Jin, Y. Zhang, F. Han and F. Wang, *Chem. Mater.*, 2024, **36**, 6347–6369.
26 N. Baumer, S. Ogi and S. Yamaguchi, *Angew. Chem., Int. Ed.*, 2025, e202501693, DOI: **10.1002/anie.202501693**.
27 A. M. Manjarres, A. Albers and G. Fernandez, *Angew. Chem., Int. Ed.*, 2025, **64**, e202419720.
28 M. P. Hendricks, K. Sato, L. C. Palmer and S. I. Stupp, *Acc. Chem. Res.*, 2017, **50**, 2440–2448.
29 M. H. Sangji, S. R. Lee, H. Sai, S. Weigand, L. C. Palmer and S. I. Stupp, *ACS Nano*, 2024, **18**, 15878–15887.
30 J. H. Ortony, B. Qiao, C. J. Newcomb, T. J. Keller, L. C. Palmer, E. Deiss-Yehiely, M. Olvera de la Cruz, S. Han and S. I. Stupp, *J. Am. Chem. Soc.*, 2017, **139**, 8915–8921.
31 H. Fu, J. Huang, J. J. B. van der Tol, L. Su, Y. Wang, S. Dey, P. Zijlstra, G. Fytas, G. Vantomme, P. Y. W. Dankers and E. W. Meijer, *Nature*, 2024, **626**, 1011–1018.
32 K. Yano, T. Hanebuchi, X. J. Zhang, Y. Itoh, Y. Uchida, T. Sato, K. Matsuura, F. Kagawa, F. Araoka and T. Aida, *J. Am. Chem. Soc.*, 2019, **141**, 10033–10038.
33 K. Yano, Y. Itoh, F. Araoka, G. Watanabe, T. Hikima and T. Aida, *Science*, 2019, **363**, 161–165.
34 X. J. Zhang, D. Morishita, T. Aoki, Y. Itoh, K. Yano, F. Araoka and T. Aida, *Chem.–Asian J.*, 2022, **17**, e202200223.
35 D. Morishita, Y. Itoh, K. Furukawa, N. Arai, X. J. Zhang and T. Aida, *Chem. Sci.*, 2024, **15**, 4068–4074.
36 M. F. J. Mabesoone, A. R. A. Palmans and E. W. Meijer, *J. Am. Chem. Soc.*, 2020, **142**, 19781–19798.
37 F. Wurthner, *J. Org. Chem.*, 2022, **87**, 1602–1615.
38 A. D. Scaccabarozzi, A. Basu, F. Anies, J. Liu, O. Zapata-Arteaga, R. Warren, Y. Firdaus, M. I. Nugraha, Y. Lin, M. Campoy-Quiles, N. Koch, C. Muller, L. Tsetseris, M. Heeney and T. D. Anthopoulos, *Chem. Rev.*, 2022, **122**, 4420–4492.
39 G. Wypych, *Handbook of Nucleating Agents*, ChemTec Publishing, Ontario, Canada, 2016.
40 C. De Rosa, M. Scoti, R. Di Girolamo, O. R. Ballesteros, F. Auriemma and A. Malafronte, *Polym. Cryst.*, 2020, **3**, e10101.
41 M. Blomenhofer, S. Ganzleben, D. Hanft, H.-W. Schmidt, M. Kristiansen, P. Smith, K. Stoll, D. Mäder and K. Hoffmann, *Macromolecules*, 2005, **38**, 3688–3695.
42 H.-W. Schmidt, P. Smith and M. Blomenhofer, *WIPO Pat.*, WO02/46300A2, 2002.
43 D. Mäder, K. Hoffmann and H.-W. Schmidt, *WIPO Pat.*, WO03/102069A1, 2003.
44 P. M. Kristiansen, A. Gress, P. Smith, D. Hanft and H.-W. Schmidt, *Polymer*, 2006, **47**, 249–253.
45 A. Thierry and B. Lotz, in *Handbook of Polymer Crystallization*, ed. E. Piorkowska and G. C. Rutledge, Wiley, Hoboken, New Jersey, 2013, pp. 237–264.
46 M. Kristiansen, P. Smith, H. Chanzy, C. Baerlocher, V. Gramlich, L. McCusker, T. Weber, P. Pattison, M. Blomenhofer and H.-W. Schmidt, *Cryst. Growth Des.*, 2009, **9**, 2556–2558.
47 C. Mathieu, A. Thierry, J. C. Wittmann and B. Lotz, *J. Polym. Sci., Part B: Polym. Phys.*, 2002, **40**, 2504–2515.
48 A. Thierry, C. Straupé, J. C. Wittmann and B. Lotz, *Macromol. Symp.*, 2006, **241**, 103–110.
49 Y. F. Zhang and Z. Xin, *J. Polym. Sci., Part B: Polym. Phys.*, 2007, **45**, 590–596.
50 H. Bai, Y. Wang, L. Liu, J. Zhang and L. Han, *J. Polym. Sci., Part B: Polym. Phys.*, 2008, **46**, 1853–1867.

51 H. Bai, Y. Wang, Q. Zhang, L. Liu and Z. Zhou, *J. Appl. Polym. Sci.*, 2008, **111**, 1624–1637.
52 Y. F. Zhang, *J. Polym. Sci., Part B: Polym. Phys.*, 2008, **46**, 911916.
53 S. Zhao and Z. Xin, *J. Polym. Sci., Part B: Polym. Phys.*, 2010, **48**, 653–665.
54 X. Li, H. Wu, J. Dai, T. Huang and Y. Wang, *J. Polym. Sci., Part B: Polym. Phys.*, 2011, **49**, 898–906.
55 Y.-F. Zhang, X.-X. Luo, L. Zhu, X.-J. Yang and Y. Chang, *J. Macromol. Sci., Part B: Phys.*, 2012, **51**, 2352–2360.
56 Q. Zhang, Z. Chen, B. Wang, J. Chen, F. Yang, J. Kang, Y. Cao, M. Xiang and H. Li, *J. Appl. Polym. Sci.*, 2014, **132**, 41355.
57 J. He, Y.-F. Zhang, X.-Q. Ren and Y. Li, *Polym. Bull.*, 2019, **76**, 5559–5575.
58 Y. F. Zhang, P. Z. Zhou and Y. Li, *Polym. Adv. Technol.*, 2019, **30**, 1777–1788.
59 A. Timme, R. Kress, R. Q. Albuquerque and H.-W. Schmidt, *Chem.–Eur. J.*, 2012, **18**, 8329–8339.
60 C. S. Zehe, J. A. Hill, N. P. Funnell, K. Kreger, K. P. van der Zwan, A. L. Goodwin, H. W. Schmidt and J. Senker, *Angew. Chem., Int. Ed.*, 2017, **56**, 4432–4437.
61 H. M. M. ten Eikelder, A. J. Markvoort, T. F. de Greef and P. A. Hilbers, *J. Phys. Chem. B*, 2012, **116**, 5291–5301.
62 H. M. M. ten Eikelder, B. Adelizzi, A. R. A. Palmans and A. J. Markvoort, *J. Phys. Chem. B*, 2019, **123**, 6627–6642.
63 H. M. M. ten Eikelder and A. J. Markvoort, *Acc. Chem. Res.*, 2019, **52**, 3465–3474.
64 M. Wehner and F. Würthner, *Nat. Rev. Chem.*, 2019, **4**, 38–53.
65 J.-M. Guenet, *Gels*, 2021, **7**, 65.
66 L. N. J. de Windt, C. Kulkarni, H. M. M. ten Eikelder, A. J. Markvoort, E. W. Meijer and A. R. A. Palmans, *Macromolecules*, 2019, **52**, 7430–7438.
67 K. Bernardino, J. Świergiel, J. Jadżyn, L. Bouteiller and A. F. de Moura, *J. Mol. Liq.*, 2019, **286**, 110937.
68 S. Cantekin, T. F. de Greef and A. R. Palmans, *Chem. Soc. Rev.*, 2012, **41**, 6125–6137.
69 C. Kulkarni, S. K. Reddy, S. J. George and S. Balasubramanian, *Chem. Phys. Lett.*, 2011, **515**, 226–230.
70 C. Kulkarni, K. K. Bejagam, S. P. Senanayak, K. S. Narayan, S. Balasubramanian and S. J. George, *J. Am. Chem. Soc.*, 2015, **137**, 3924–3932.
71 Y. Matsunaga, N. Miyajima, Y. Nakayasu and S. Sakai, *Bull. Chem. Soc. Jpn.*, 1988, **61**, 207–210.
72 C. F. C. Fitié, I. Tomatsu, D. Byelov, W. H. de Jeu and R. P. Sijbesma, *Chem. Mater.*, 2008, **20**, 2394–2404.
73 G. Odian, *Principles of Polymerization*, Wiley, Hoboken, New Jersey, 2004.
74 B. Lotz and J. C. Wittmann, in *Solidification Processes in Polymers. Progress in Colloid & Polymer Science*, ed. J. F. Janssson and U. W. Gedde, Steinkopff, 1992, vol. 87, pp. 3–7.
75 B. Lotz, *Polymer*, 1998, **39**, 4561–4567.
76 F. García, R. Gómez and L. Sánchez, *Chem. Soc. Rev.*, 2023, **52**, 7524–7548.